

A size-dependent crystal plasticity finite-element model for creep and load shedding in polycrystalline titanium alloys

G. Venkatramani, S. Ghosh ^{*}, M. Mills

Department of Mechanical Engineering, Ohio State University, Room W496, Scott Laboratory, 201 West 19th Avenue, Columbus, OH 43210, USA

Received 5 January 2007; received in revised form 6 March 2007; accepted 11 March 2007

Available online 8 May 2007

Abstract

A rate-dependent anisotropic elastic-crystal plasticity based finite-element (FE) model with size-dependent yield strength is developed for polycrystalline Ti-6242. The initial slip system deformation resistances in the crystal plasticity relations are expressed as Hall–Petch type relations, where the grain size, lath size and colony size are chosen as characteristic lengths depending on the nature of slip. The FE model incorporates accurate phase volume fractions and orientation distributions that are statistically equivalent to those observed in orientation imaging microscopy (OIM) maps of the microstructure. The model is validated with experimental results on constant strain rate and creep tests. A relationship between the macroscopic flow stress and grain size and lath size for two-phase Ti-6242 is proposed. The effect of grain morphology on creep-induced load shedding and localization is discussed.

© 2007 Acta Materialia Inc. Published by Elsevier Ltd. All rights reserved.

Keywords: Ti-6242; Size-dependent crystal plasticity; Load shedding; 3D microstructure model

1. Introduction

Two-phase α/β titanium alloys such as Ti-6242 possess various desirable properties such as high specific strength, elastic modulus and fracture toughness, which make them suitable for a wide range of applications in the aerospace, orthopedic, dental and sporting goods industries [1]. However, structural components made of α/β titanium alloys have exhibited premature failure when subjected to dwell cyclic loading, in which the load cycle includes a hold period. Experimental studies on dwell and normal fatigue have demonstrated that dwell specimens show marked reduction in the number of cycles to failure compared with the pure fatigue specimens [2]. The dwell sensitivity has been attributed to a deleterious mechanism of cold-creep or strain accumulation, in which significant time-dependent strain accumulates under static applied stresses that are lower than or equal to yield strength. These observations suggest

that time-dependent strain accumulation due to creep is a critical factor in understanding failure mechanisms in dwell fatigue. Of particular interest is the role of microstructure on the local load shedding, caused by this local accumulated strain. Various phenomenological models of fatigue life [3] fail to account for the dependence of local plastic deformation and load shedding on microstructural parameters, such as grain size, shape and slip system orientation. Time-dependent plastic deformation in Ti alloys has considerable dependence on grain orientation due to the low symmetry of the predominant hcp α -phase. The relative strength of neighboring grains is also highly dependent on the orientation of basal planes with respect to the axis of loading. Large local stress concentrations are found to develop in $\langle c + a \rangle$ oriented grains due to local load shedding from neighboring softer $\langle a \rangle$ oriented grains, resulting in crack initiation [4]. Hence, the study of dwell fatigue phenomena in two-phase Ti-6242 alloys requires special focus on creep due to time-dependent accumulation of plastic strain and the load shedding phenomena of stress redistribution, consistent with grain orientation and morphology.

^{*} Corresponding author. Tel.: +1 614 292 2599; fax: +1 614 292 3163.
E-mail address: ghosh.5@osu.edu (S. Ghosh).

The present study is aimed at understanding the effects of microstructural parameters on the deformation and creep response of polycrystalline Ti-6242 through finite-element (FE) simulations. The microstructure of Ti-6242 alloy, shown in Fig. 1, consists of transformed β colonies with an alternating arrangement of α (hexagonal close packed or hcp) and β (body centered cubic or bcc) lamellae in a matrix of equiaxed primary α (hcp) grains. The corresponding composition is given in Table 1. A large strain FE model for Ti-6242, incorporating a rate-dependent anisotropic crystal plasticity constitutive model has been developed by the authors in Ref. [5]. The model accounts for microstructural morphology through accurate phase volume fractions, and orientation distributions that are statistically equivalent to those observed in orientation imaging microscopy (OIM) scans. An effective homogenized model is developed using Taylor's assumptions for the $\alpha + \beta$ transformed β phase colony regions. Material properties for each of the constituent phases and individual slip systems in the crystal plasticity model are calibrated from single crystal and single colony experimental results by a genetic algorithm (GA) based minimization scheme. The model accounts for experimentally observed tension–compression asymmetry through different values of crystal plasticity parameters in individual slip systems. Fig. 2 shows the result of a simulation of compression creep for polycrystalline Ti-6242 using crystal plasticity parameters calibrated for single crystal primary α and single colony transformed β phases in Refs. [5,6]. Results of the simulation, conducted for 95.5% yield stress, are compared with experiments in the figure. The simulation is not able to predict the experimental results well, since the effect of grain size is not accounted for in the strengthening of the polycrystalline sample. To incorporate the grain size effect,

the calibrated slip system deformation resistance parameters were adjusted in an ad hoc manner in Ref. [5] to match macroscopic experimental results. However, this method is not physically based. It fails to account for the mean free path traversed by dislocations and the differences between individual slip transmission in a complex two-phase system, where the strengthening effect may be due to dislocation pile-up at the grain, lath or colony boundary, depending on slip direction. A more physical approach is proposed in the present study to incorporate the size effect in slip system strengthening and to predict the slip system deformation parameters of individual slip systems as functions of the grain size, colony size or lath size.

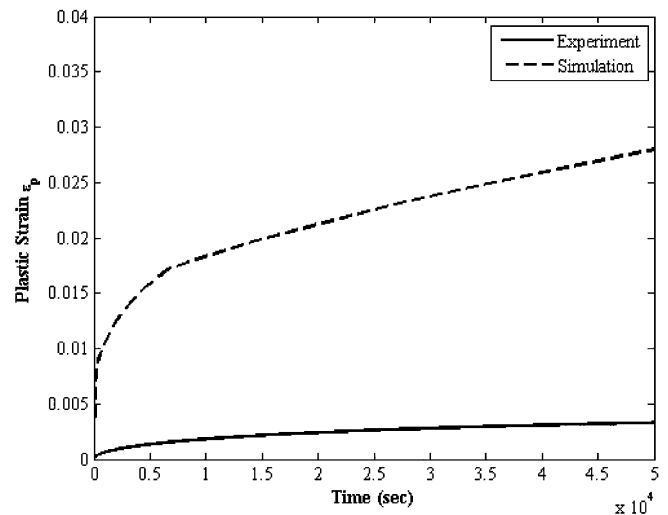


Fig. 2. Creep strain evolution from experiments and simulations with the single colony and single crystal parameters without any size-effect adjustment, for a stress level of 907 MPa in compression.

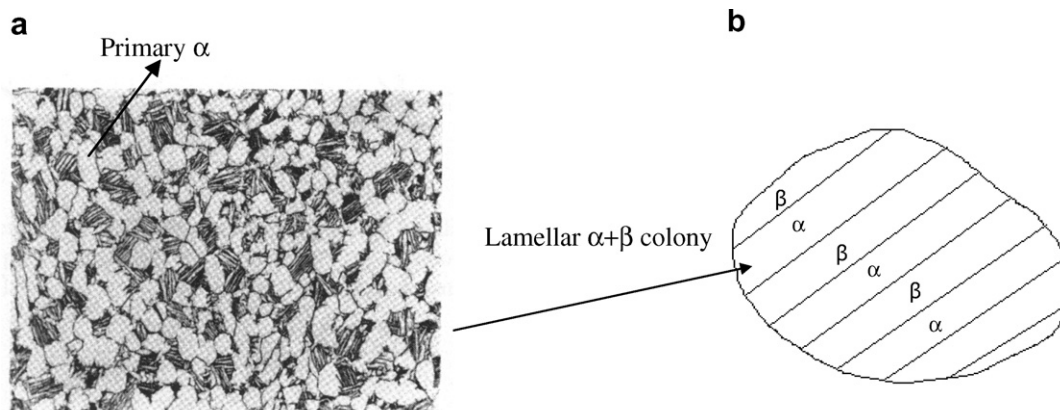


Fig. 1. (a) Microstructure of a forged $\alpha + \beta$ Ti-6242 alloy consisting of transformed β (dark phase) colonies in a matrix of equiaxed primary α grains (light phase); (b) schematic of a constituent transformed β colony.

Table 1
Chemical composition of Ti-6242

| Alloy | Al (wt.%) | Mo (wt.%) | Sn (wt.%) | Zr (wt.%) | Si (wt.%) | O (wt.%) | N (wt.%) | Ti (wt.%) |
|---------|-----------|-----------|-----------|-----------|-----------|----------|----------|-----------|
| Ti-6242 | 6.01 | 1.96 | 1.96 | 4.01 | 0.10 | 0.131 | 0.012 | 85.817 |

The dependence of flow stress on grain size was proposed in the early 1950s by Hall and Petch [7,8] as being due to grain boundary strengthening. Experimental studies on titanium alloys have shown grain and lath size–effect strengthening following a Hall–Petch type relation. Some of this work has expanded the inverse square root relationship relating the grain size and flow stress to include strengthening due to lath boundaries for multiphase alloys. The effect due to grain and lath size of fully lamellar Ti–45.5Al–2Cr–1.5Nb–1V was studied by Cao et al. [9] who showed that the yield strength increases with decreasing grain size and lamellar spacing. The effect of α platelet thickness on plastic flow of Ti–6Al–4V with a transformed microstructure was studied by Semiaton and Bieler [10] at hot working temperatures. In this study, the α thickness was varied from 0.4 to 10 μm , keeping the β thickness constant and the Hall–Petch dependence of flow stress at higher temperature was demonstrated. An important observation with respect to size-induced strengthening is flow-stress saturation at a threshold value of grain size. The effect of lamellar spacing on the mechanical properties of Ti–Al alloy at room and high temperatures was studied by Maruyama et al. [11] by varying the lamellar spacing from 20 to 590 nm, while keeping the grain size constant. The validity of the Hall–Petch relationship between lamellar spacing and yield stress of the alloy with a saturation threshold was shown through a pile-up model of dislocations at lamellar interfaces. Mills and Norfleet [12] have also observed strengthening with smaller lath size in their experiments with β processed Ti–6Al–4V and Ti-6242, making the in situ phases relatively stronger.

A rate-dependent anisotropic elastic-crystal plasticity constitutive model with size-dependent yield strength is proposed in this paper for polycrystalline Ti-6242. The

model relates slip system deformation resistance with the grain size, colony size and lath size in the microstructure, using different characteristic lengths for different slip systems in the primary α and transformed β regions based on the slip direction. Thus, the initial slip system deformation resistances in the crystal plasticity relations are expressed as Hall–Petch type relations found in the literature [9–11], based on models of dislocation pile-up for various deformation modes. The size–effect parameters are determined from single crystal and colony experiments discussed in Refs. [5,6]. The model is validated by comparing the results of simulation with those from constant strain rate and creep tests on polyphase-polycrystalline Ti-6242. The validated model is further used to obtain macroscopic flow stress dependence on grain size and lath size in Ti-6242 through constant strain rate simulations. It is also used to understand the effect of grain size and shape on load shedding between hard and soft oriented grains. Numerical simulations are subsequently carried out on a three-dimensional (3D) microstructure that is created as a statistical equivalent to a real microstructure. The importance of accurate representation of grain size distribution in the identification of local hot spots crucial for dwell fatigue crack initiation is emphasized.

2. Material description

An optical micrograph of forged α/β Ti-6242 material is shown in Fig. 1a. As shown in Fig. 3a, the hcp crystals consist of five different families of slip systems, namely basal $\langle a \rangle$, prismatic $\langle a \rangle$, pyramidal $\langle a \rangle$, first-order pyramidal $\langle c+a \rangle$ and second-order pyramidal $\langle c+a \rangle$, with a total of 30 possible slip systems. A transversely isotropic elastic response is assumed for these crystals with five independent constants. The bcc crystal system consists

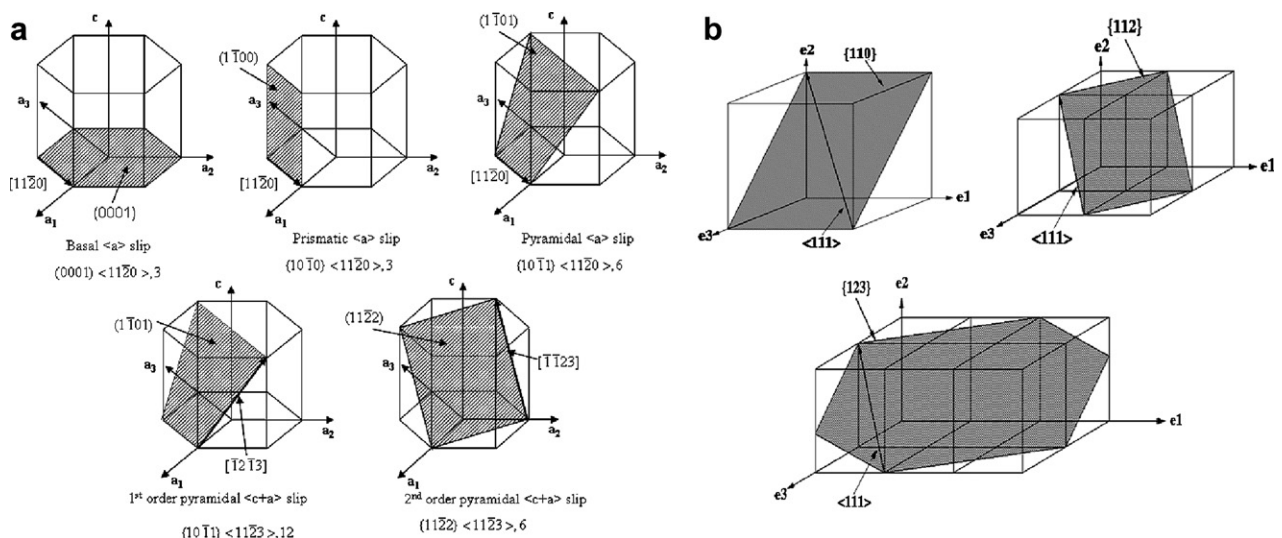


Fig. 3. Schematic diagrams showing (a) the non-orthogonal basis and slip systems in a hcp crystal and (b) the orthogonal basis and slip systems in bcc crystals.

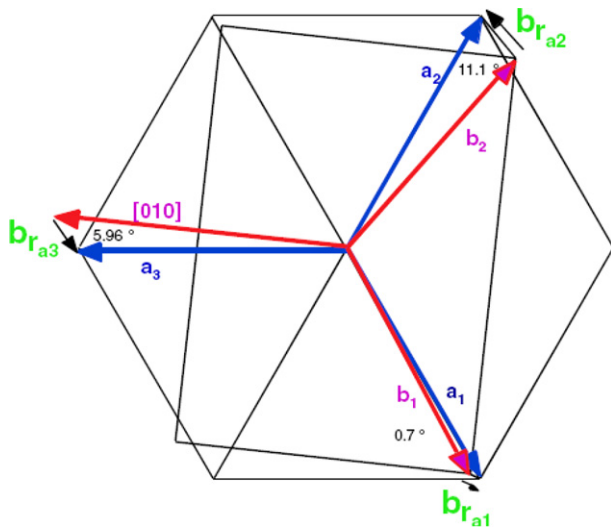


Fig. 4. Burgers orientation relationship in the transformed β phase of Ti-6242 that brings the hcp a_1 ($[2\bar{1}\bar{1}0]$) slip direction in alignment with the bcc b_1 slip direction.

of three different slip families, $\langle 111 \rangle \{110\}$, $\langle 111 \rangle \{112\}$ and $\langle 111 \rangle \{123\}$, with a total of 48 slip systems as shown in Fig. 3b. A cubic symmetric elastic matrix is assumed for the bcc material with three independent constants. For the specimens analyzed, the volume fraction of the transformed β phase in the Ti-6242 material microstructure was 30%. Within the transformed β colonies, the α and β lamellae were experimentally observed to have volume fractions of $\sim 88\%$ and 12%, respectively [13]. The orientations of α and β lamellae follow a Burgers orientation relationship [14] that is expressed as $(101)_\beta \parallel (0001)_\alpha$, $[1\bar{1}\bar{1}]_\beta \parallel [2\bar{1}\bar{1}0]_\alpha$. This relation brings the hcp a_1 ($[2\bar{1}\bar{1}0]$) slip direction in alignment with the bcc b_1 slip direction, as shown in Fig. 4.

3. Size effect in crystal plasticity

The deformation behavior of individual phases of the Ti-6242 microstructure is modeled using an isothermal, rate-dependent, finite-strain elastic-crystal plastic constitutive relation that is described in Ref. [15]. The flow rule governing evolution of plastic deformation is expressed in terms of the plastic velocity gradient as

$$L^p = \dot{\mathbf{F}}^p \mathbf{F}^{p-1} = \sum_{\alpha} \dot{\gamma}^{\alpha} \mathbf{s}_0^{\alpha}, \dot{\gamma}^{\alpha} = \dot{\gamma} \left| \frac{\tau^{\alpha}}{g^{\alpha}} \right|^{1/m} \text{sign}(\tau^{\alpha}) \quad (1)$$

where the α th slip system Schmid tensor is expressed as $\mathbf{s}_0^{\alpha} \equiv \mathbf{m}_0^{\alpha} \otimes \mathbf{n}_0^{\alpha}$ in terms of the slip direction \mathbf{m}_0^{α} and slip plane normal \mathbf{n}_0^{α} in the reference configuration, $\dot{\gamma}^{\alpha}$ is plastic shearing rate on the α th slip system, τ^{α} and g^{α} are the α th slip system resolved shear stress and the slip system deformation resistance, respectively, and m is the material rate sensitivity parameter. The evolution of the slip system deformation resistance g^{α} and the hardening rates for hcp

and bcc are as given in Refs. [16,17], respectively. A back-stress is included in the power law of Eq. (1) to model cyclic deformation with kinematic hardening and is explained in detail in Ref. [6]. For the transformed β colony an equivalent homogenized crystal plasticity model of the $\alpha + \beta$ or transformed β phase colony regions has been developed [5]. The equivalent model consists of 78 slip systems, of which 30 correspond to hcp (secondary α) and 48 correspond to bcc slip systems, for which the α and β lamellae are aligned following the Burgers orientation relationship. Assumptions for a Taylor model are made in the construction of the equivalent crystal, i.e., a uniform deformation gradient F_{ij} is assumed for the two phases in the transformed β colonies. The true stress tensor at a material point for the equivalent crystal is determined using the rule of mixtures, in which a weighted averaging of the individual phase stresses is conducted with phase volume fractions as weights. Since the volume fraction of the bcc phase in the transformed β colony is relatively small ($\sim 12\%$), the rule of mixtures based model is deemed adequate. The crystal plasticity code is implemented in the commercial FE code MSC MARC [18] using the user-defined material routine HYPELA2; the implementation and calibration of material parameters have been discussed in detail in Refs. [5,6].

In continuum plasticity, the dependence of the flow stress on the grain size has been expressed by the Hall–Petch relationship in Refs. [7,8]. In crystal plasticity formulation, a similar equation that relates the slip system deformation resistance g^{α} to a characteristic size can be expressed as

$$g^{\alpha} = g_0^{\alpha} + \frac{K^{\alpha}}{\sqrt{D^{\alpha}}} \quad (2)$$

where g_0^{α} and K^{α} are size-effect-related slip system constants that refer to the interior slip system deformation resistance and slope, respectively, and D^{α} is the characteristic length scale governing the size effect. While the characteristic length scale (D^{α}) for a single-phase alloy is conventionally represented by the average grain size, it is more complex in the case of a multi-phase material such as Ti-6242 consisting of single phase primary α and dual phase transformed β regions. In this case, the grain size, colony size and α and β lath thicknesses in the colony can all serve as different length scales governing the size effect. Moreover, the ease of α/β slip transmission for a_1 , a_2 and a_3 basal and prismatic slips in the transformed β region varies significantly due to varying misalignment between the corresponding slips in the α and β phases. This causes anisotropy in the critical resolved shear stress (CRSS) and, hence, the slip system deformation resistance g^{α} . This anisotropy in CRSS is incorporated by a size-effect relationship with a particular characteristic length, such as colony size or lath size for the transformed β region to obtain the slip system deformation resistance g^{α} of the α th slip system.

3.1. Slip transmission and characteristic lengths

In the transformed β regions, three different characteristic length scales are considered, namely the colony size D_s , the α lath thickness l_α , and the β lath thickness l_β . The plastic deformation is activated through two types of slip modes, namely the hard and soft slip modes, as illustrated in Fig. 5a and b, respectively. Identification of these slip modes in the transformed β region is based on the work of Savage et al. [13,19], in which the misorientation angles between slips in α and β phases are used to describe the anisotropy in the CRSS. The orientations of α and β lamellae follow a Burgers orientation relationship, which brings the hcp a_1 ($[2\bar{1}\bar{1}0]$) slip direction into coincidence with the bcc b_1 slip, resulting in a relatively easy slip transmission across the interface, as shown in Fig. 4. The soft slip mode corresponds to systems in which the dislocations glide or slip parallel to the interface or transmit freely across the α/β interface due to the presence of a common slip system between the two phases. The a_1 slip direction of the basal and prism and b_1 slip directions of bcc are classified as soft slip modes. The resistance to slip in the soft slip mode is only from the colony boundary and, hence, the colony size D_s is the characteristic length for the size effect. The hard slip mode, on the other hand, corresponds to systems in which the slip transmission is impeded by the α/β interface due to the absence of a common slip system between the α and β phases. There is a significant misalignment between the α phase a_2 ($[\bar{1}2\bar{1}0]$) and β phase b_2 slip directions, and also between the a_3 ($[\bar{1}\bar{1}20]$) and all $\langle 111 \rangle_\beta$ directions in the β phase. Consequently, the barrier to dislocation motion across the interface is sufficiently large that dislocation pile-ups are developed for these slips and, hence, are classified as hard slip modes. Correspondingly in the β phase, any slip directions other than b_1 ($[\bar{1}11]$) are expected to be impeded by the lath boundary and are classified as hard slip modes. Thus the characteristic lengths for systems with hard slip modes are l_α and l_β for the hcp and bcc phases, respectively. In the case of the primary α region, the grain boundary retards the transmission of slip for all systems. These systems correspond to soft slip modes with

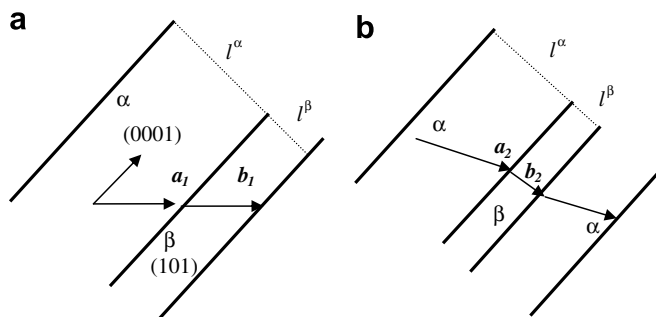


Fig. 5. Slip modes at the α/β interface in the transformed β phase of Ti-6242: (a) soft slip mode showing presence of common slip a_1 and b_1 ; (b) hard slip mode showing large misorientation between a_2 and b_2 .

Table 2

Characteristic length scale, D^z , governing the size effect for various slip systems

| | Slip system | Characteristic length | Deformation mode |
|---------------------------|-------------------|-----------------------|------------------|
| Transformed β (hcp) | a_1 basal | D_c | Soft |
| | a_2 basal | l_α | Hard |
| | a_3 basal | l_α | Hard |
| | a_1 prism | D_c | Soft |
| | a_2 prism | l_α | Hard |
| | a_3 prism | l_α | Hard |
| Primary α | All systems | D_g | Soft |
| Transformed β (bcc) | $b_1[\bar{1}11]$ | D_c | Soft |
| | All other systems | l_β | Hard |

D_c , colony size; D_g , grain size; l_α , α lath thickness; l_β , β lath thickness.

the grain size D_g as the characteristic length. Characteristic lengths used in the size–effect relationship for different systems of primary α and transformed β are summarized in Table 2.

3.2. Crystal plasticity constants for incorporating the size effect

The next step is to obtain the constants g_0^z , K_h^z and K_s^z in Eq. (2) for the crystal plasticity relation incorporating size effects. The internal grain strength g_0^z is obtained from the g^z values calibrated from single crystal and single colony experiments [5] for primary α and transformed β regions, respectively. The single colony experiments were conducted on samples of α/β colonies of Ti-6242 as detailed in Ref. [13]. The calibrated values for the transformed β region reflect the anisotropy of the three basal and prismatic systems. While the slip system deformation resistance g_0^z is the same, the anisotropy is attributed to different values of the second size–effect term in Eq. (2), arising out of dislocation pile-up at the lath boundary. The constants K_h^z or K_s^z corresponding to the Hall–Petch slope of the $g^z - \frac{1}{\sqrt{D^z}}$ plot are based on the dislocation pile-up model for hard and soft modes of slip. This is explained next.

3.2.1. Determination of K for the soft slip mode

In the primary α and transformed β regions, the expression for the Hall–Petch slope K_s^z of the $g^z - \frac{1}{\sqrt{D^z}}$ plot corresponding to soft slip modes is given in Refs. [9,20] as

$$K_s^z = \sqrt{\frac{(2-v)\pi\tau^*Gb}{2(1-v)}} \quad (3)$$

where v is the Poisson's ratio, G is the shear modulus, b is the Burgers vector and τ^* is the barrier strength for the grain boundary, which is taken as $0.01 G$ for the soft slip mode. The expression (3) has been obtained in Ref. [20] by solving the problem of a circular crack under shear to obtain an equilibrated distribution function for circular dislocations within a circular domain. In the present study, the G values are those calibrated from single colonies and

Table 3

Values of constants used in the determination of K_h^α and K_s^α in the Hall–Petch relations

| | |
|--------------------------------|-----------|
| G (primary α) | 48.0 GPa |
| G (transformed β -hcp) | 43.0 GPa |
| G (transformed β -bcc) | 115.0 GPa |
| b (hcp) | 0.30 nm |
| b (bcc) | 0.33 nm |
| ν | 0.33 |
| α | 0.835 |

single crystals for the transformed β and primary α regions, respectively, in Refs. [5,6]. Values of the various constants are summarized in Table 3.

3.2.2. Determination of K for the hard slip mode

In the hard slip mode, the value of slope K_h^α is based on an expression for strengthening due to dislocation pile-ups at the interface, developed by Eshelby [10,21] and is given as

$$K_h^\alpha = \sqrt{\frac{4\tau^*Gb}{\alpha\pi}} \quad (4)$$

where α is a constant taken as 1.0 for screw dislocations and $(1 - \nu)$ for edge dislocations. The expression for the slope K_h^α has been obtained in Ref. [21] by considering dislocation pile-ups in an elliptical barrier as opposed to the circular boundary for grain boundary strengthening considered in Section 3.2.1. The stress concentration due to pile-up is obtained from the equilibrated number of dislocations for an elliptical crack under shear loading, from which the slope K_h^α can be derived. The expression based on the elliptical barrier is used for lath boundary strengthening, while that based on the circular barrier is used for grain boundary strengthening. In the present study, the screw and edge dislocations are taken to be 50% each and, hence, $\alpha = \frac{1}{2}[1 + (1 - \nu)]$. The barrier strength τ^* for the hard slip mode is obtained from calibrated values for the corresponding slip systems, which reflects the strengthening due to the size effect. This is explained below.

3.2.3. Determination of g_0^α for the transformed β phase

The calibrated values of the initial slip system deformation resistance, g^α , in Ref. [5] reflect the anisotropy exhibited by the three basal and prism slip systems and also the asymmetry between the tension and compression observed in the single colonies of α/β Ti-6242. The tension–compression asymmetry has been attributed to one or a combination of a number of mechanisms, namely residual stresses in single colonies due to the growth process, elastic stress fields at the α/β interface aiding or impairing slip transmission, effects on the mobility of $\langle a \rangle$ type dislocations in the α phase, and effects on the mobility of dislocations in the β phase and differing slip transmission mechanisms based on the direction of loading [13]. Tension–compression asymmetry is incorporated in the

Table 4

Calibrated values of slip system deformation resistance (g^α) for secondary α basal and prism $\langle a \rangle$ slip systems in compression and tension

| | a_1 basal | a_2 basal | a_3 basal | a_1 prism | a_2 prism | a_3 prism |
|--------------------|-------------|-------------|-------------|-------------|-------------|-------------|
| <i>Compression</i> | | | | | | |
| g^α | 385.0 | 445.0 | 450.0 | – | – | – |
| <i>Tension</i> | | | | | | |
| g^α | 284.0 | 315 | 243 | 240.0 | 245.0 | 255.0 |

crystal plasticity model by using a criterion based on the sign of the maximum principal stress at a given point. These values, presented in Table 4 for various slip systems in tension and compression, are also used to determine the constant g_0 for different slip systems.

The g^α values of the a_1 basal and prism systems of a single transformed β colony correspond to the g_0^α values of these systems in Eq. (2), since the resistance to slip is provided only by the colony boundary corresponding to the infinite characteristic length D^α in a single colony. In the case of a_2 and a_3 basal and prism systems the lath boundary impedes the slip transmission between the two phases and, hence, the calibrated value is assumed to reflect this strengthening. As seen in Table 4, the values corresponding to hard slip mode systems are higher than those of soft slip mode systems in tension as well as compression, except for the a_3 basal system, which is ignored. The barrier strength and the slope K_h^α for the hard slip mode are obtained by substituting the l_α of the hcp phase and the g_0^α obtained for the a_1 basal system into Eq. (2). The barrier strength, τ^* , for soft deformation is assumed as $0.01G$, from which the constants K_h^α and K_s^α can be obtained for different systems in tension and compression. Thus the anisotropy in the slip system deformation values is accounted for with the same deformation resistance g_0^α and different slopes K_h^α and K_s^α in the Hall–Petch relation. Similarly, the calibrated values for the single colony bcc phase are used to obtain the g_0^α values of the b_1 system, which has resistance only from the colony boundary. For the other bcc phase slip systems that have resistance from the lath boundary, a barrier strength of $0.015G$ is assumed to determine K_h^α , as proposed in Refs. [10,21]. Slip systems for which direct experimental single colony results are not available include the three $\langle a \rangle$ prisms in compression. For these systems, the values are obtained by assuming the same basal-to-prismatic ratio as that observed in the single crystal results of Ti-6Al in compression. The lath sizes and average grain

Table 5

Grain size and lath size of single colony and polycrystalline experimental samples

| | |
|----------------------------|--------------------|
| l_α (single colony) | 10 μm |
| l_β (single colony) | 2 μm |
| l_α (polycrystal) | 1 μm |
| l_β (polycrystal) | 0.35 μm |
| $D_g = D_c$ | 5 μm |

Table 6

Values of Hall–Petch constants (g_0 and K) and g^α of hcp slip systems in polycrystalline Ti-6242 in tension obtained from the size–effect relationship

| | a_1 basal | a_2 basal | a_3 basal | a_1 prism | a_2 prism | a_3 prism |
|--|-------------|-------------|-------------|-------------|-------------|-------------|
| <i>Primary α</i> | | | | | | |
| g_0 | 284.0 | 284.0 | 284.0 | 282.2 | 282.2 | 282.2 |
| K | 164.5 | 164.5 | 164.5 | 164.5 | 164.5 | 164.5 |
| g^α | 357.6 | 357.6 | 357.6 | 355.8 | 355.8 | 355.8 |
| <i>Transformed βhcp</i> | | | | | | |
| g_0 | 284.0 | 284.0 | 284.0 | 240.0 | 240.0 | 240.0 |
| K | 147.4 | 98.0 | 98.0 | 147.4 | 15.8 | 47.4 |
| g^α | 349.9 | 382.0 | 382.0 | 305.9 | 255.8 | 287.4 |

Table 7

Values of Hall–Petch constants (g_0 and K) and g^α of hcp slip systems in polycrystalline Ti-6242 in compression, obtained from the size–effect relationship

| | a_1 basal | a_2 basal | a_3 basal | a_1 prism | a_2 prism | a_3 prism |
|--|-------------|-------------|-------------|-------------|-------------|-------------|
| <i>Primary α</i> | | | | | | |
| g_0 | 322.0 | 322.0 | 322.0 | 320.0 | 320.0 | 320.0 |
| K | 164.5 | 164.5 | 164.5 | 164.5 | 164.5 | 164.5 |
| g^α | 395.6 | 395.6 | 395.6 | 393.6 | 393.6 | 393.6 |
| <i>Transformed βhcp</i> | | | | | | |
| g_0 | 385.0 | 385.0 | 385.0 | 382.6 | 382.6 | 382.6 |
| K | 147.4 | 189.7 | 205.5 | 147.4 | 188.5 | 204.3 |
| g^α | 450.9 | 574.7 | 590.6 | 448.5 | 571.1 | 586.9 |

sizes of single colony samples are presented in Table 5 and the Hall–Petch parameters for tension and compression are given in Tables 6 and 7, respectively.

3.2.4. Determination of g_0 for the primary α phase

The crystal plasticity parameters, calibrated for single crystal α Ti–6Al [6], are used in the present study for the primary α phase. Due to the absence of any β phase, the three $\langle a \rangle$ type slip vectors are not unique in the primary α regions and identical parameters are assigned to all of them. Values of g^α that are calibrated for individual systems in the compression experiments directly give the g_0^α values in Eq. (2), since there is no resistance to slip due to the grain boundary. From the g_0^α values and the values of K_s^α obtained from Eq. (3), the g^α value of any grain size can be obtained by using the Hall–Petch relationship of Eq. (2). Tension–compression asymmetry observed in single crystal Ti–6Al in Ref. [22] has to be taken into account while assuming the initial g_0^α values of primary α in tension, since direct experimental results are not available. It is reasonable to assume the calibrated value of g^α of the a_1 basal of the transformed β single colony for the three $\langle a \rangle$ basals of primary α in tension, since this slip does not have any resistance to the lath boundary. The ratio of the basal to g_0^α in compression is also assumed for tension and the values of the three $\langle a \rangle$ prisms in tension are thus obtained.

3.2.5. Saturation lath size for size–effect

It has been shown in Ref. [11] that the Hall–Petch relationship for lamellar structures reaches a saturation value at a critical lamellar spacing that is explained by the pile-up model of dislocations at lamellar interfaces. The critical lamellar spacing, λ^* , below which there is no further strengthening, is given as [11]:

$$\lambda^* = \frac{Gb}{(1-\nu)\tau^*} \quad (5)$$

This limiting value λ^* is incorporated for the characteristic lath thicknesses l_α and l_β for calculation of the saturation g^α values.

4. FE simulation of creep and constant strain rate tests

Numerical simulations are carried out in this section for specimens of polycrystalline Ti-6242 using the size-dependent crystal plasticity model and compared with the results of constant strain rate and creep experiments in tension and compression. The in situ α/β laths in the transformed β phase of polycrystalline Ti-6242 are of significantly reduced size (much finer) in comparison with the single colony samples of Ti-6242 [5] (see Table 5). There is a strong effect of grain size on the flow stress in the polycrystalline sample. The crystal plasticity parameters calibrated from single crystal and single colony tests are scaled in accordance with the flow–stress–size relations, prior to their use in the polycrystalline models using the Hall–Petch model discussed in Section 3.2. The lath sizes and average grain sizes of the single and polycrystalline samples are presented in Table 5. The corresponding size-scaled values of g^α for the primary α and transformed β phases for tension and compression, respectively, are summarized in Tables 6 and 7. Properties of the bcc phase are listed in Table 8. Other calibrated values of g^α , for which direct experimental data are not available, are 625 MPa for the $\langle c+a \rangle$ pyramidal tension test and 675 MPa for the $\langle c+a \rangle$ pyramidal compression test. This gives a pyramidal/basal ratio of ~ 2 .

Table 8

Values of Hall–Petch constants (g_0 and K) and g^α of bcc slip systems in polycrystalline Ti-6242, obtained from the size–effect relationship

| | {101} | {112} hard | {112} soft | {123} hard | {123} soft |
|---------------------------------------|-------|---------------|---------------|---------------|---------------|
| <i>Transformed β</i> | | | | | |
| g_0 (b_1) | 250.0 | 229.8 | 209.6 | 251.3 | 200.6 |
| g^α (b_1) | 434.9 | 414.7 | 394.5 | 436.1 | 385.5 |
| K_s | 413.4 | | K_h | 315.9 | |
| g_0 (other than b_1) | 0.0 | 0.0 | 0.0 | 0.0 | 0.0 |
| g^α (other than b_1) | 534.1 | 534.1 | 534.1 | 534.1 | 534.1 |

4.1. Validation of the Ti-6242 model for constant strain rate and creep tests

Simulations of two types of mechanical tests – namely (i) tensile and compressive constant strain rate tests and (ii) tensile and compressive creep tests – are conducted with the size-dependent crystal plasticity model. The corresponding mechanical tests on Ti-6242 polycrystals have been discussed in Ref. [22]. Constant strain rate compression samples were tested at room temperature at $1 \times 10^{-4} \text{ s}^{-1}$ using an Instron 1362 mechanical test frame equipped with a compression cage. Creep samples were tested using an ATS 20 kips dead load creep frame at a stress of 95.5% of the engineering yield stress of the material ($\sim 907 \text{ MPa}$). The tensile constant strain rate tests were carried out at $1.114 \times 10^{-4} \text{ s}^{-1}$ in a closed loop servo-hydraulic test frame. The tensile dead load creep test was performed at an engineering stress of 897 MPa.

4.1.1. The FE model of polycrystalline Ti-6242

The FE model of the polycrystalline aggregate consists of a unit cubic domain that is discretized into 2744 eight-noded tri-linear brick elements in the commercial FE code MARC [18]. Each element in the FE representation of polycrystalline Ti-6242 aggregate, shown in Fig. 6c, represents a single α grain or a transformed β grain ($\alpha + \beta$ colony). For physically meaningful simulations, it is important to assign appropriate crystallographic orientations to the elements in the FE model that are statistically equivalent to those obtained from OIM. Texture assignment to the FE model involves three main steps delineated as: (a) orientation assignment using the orientation probability assignment method (OPAM); (b) misorientation assignment using the misorientation probability assignment method (MPAM); and (c) microtexture assignment using the microtexture probability assignment method (MTPAM). The probability assignment methods invoke

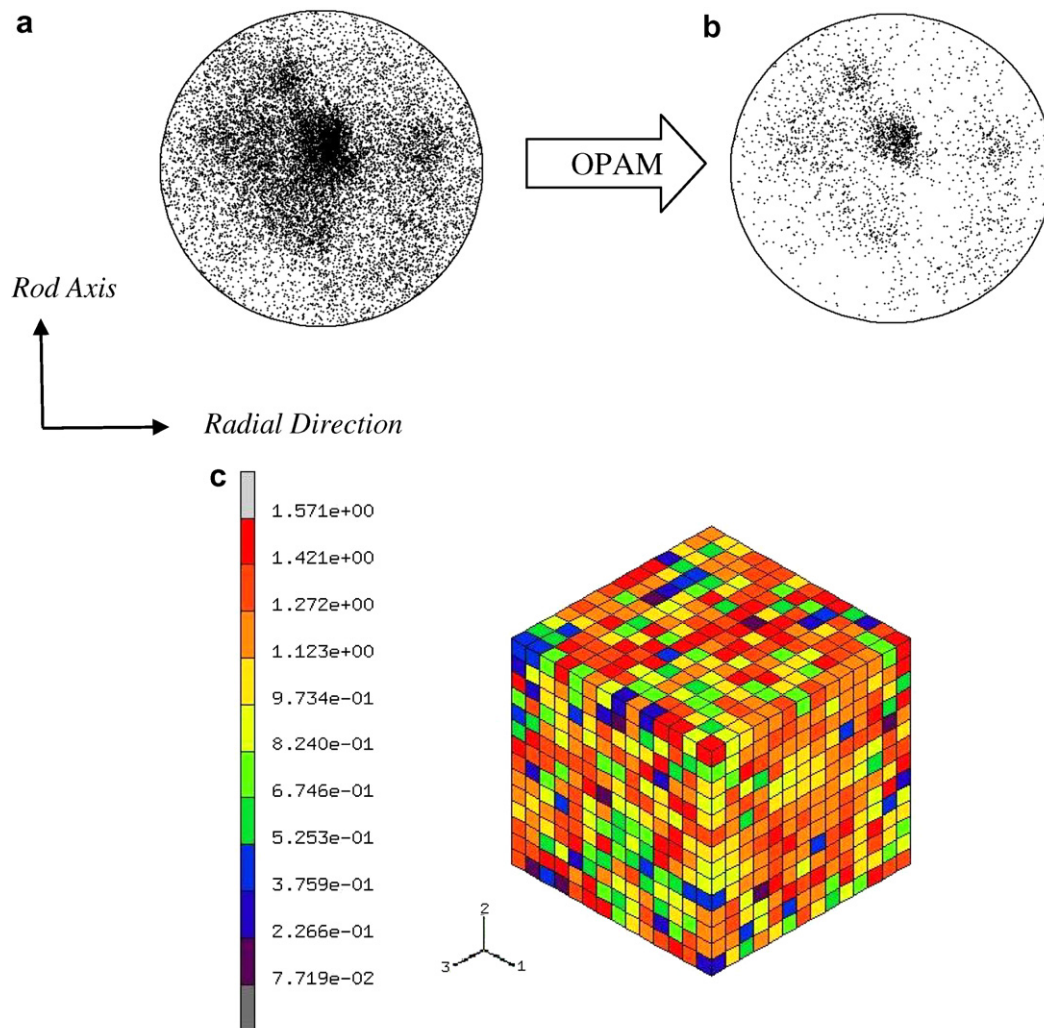


Fig. 6. Orientation assignment to the FE mesh: (a) experimentally observed (0001) pole figure with 14,799 points; (b) (0001) pole figure with 2744 points assigned to the FE model; (c) FE model showing element orientations of polycrystalline Ti-6242 model; the color represents the angle between the 'c'-axis of the grain and the loading axis in radians. (For interpretation of the references to colour in this figure legend, the reader is referred to the web version of this article.)

iterations to statistically match experimentally observed orientation distributions and these three steps have been discussed in detail in Refs. [5,26]. Experimentally measured (0001) pole figures with 14,799 orientations are compared with 2744 orientations assigned by OPAM in the simulated microstructure in Fig. 6a and b. The FE model with statistically equivalent orientation, misorientation and microtexture distributions to those observed in OIM scans is shown in Fig. 6c. In this model, 70% of the grains are primary α with hcp crystal structure and the remaining 30% are transformed β grains represented by the homogenized equivalent model. To simulate the constant strain rate tests, a displacement boundary condition was applied to the top face of the unit cube as $u(t) = l_0(\exp(\dot{\epsilon}_c t) - 1)$, where l_0 is the initial dimension of the cube and $\dot{\epsilon}_c$ is the applied strain rate. To simulate the creep experiments, a uniform pressure boundary was applied to the top face and ramped from zero to the desired creep load in an interval of 1 s, using the FORCEM routine of MARC [18].

4.1.2. Validation results

The average simulated stress–strain responses for the constant strain rate tests are plotted in Fig. 7a and b for compression and tension, respectively, and compared with experimental results. In the Figure, σ_{22} and ϵ_{22} refer to the volume-averaged Cauchy stress and the total strain, respectively, in the direction of the applied displacement. Similarly, the volume-averaged simulated plastic strain is plotted as a function of time and compared with the results of the creep experiments in Fig. 8a and b for compression and tension, respectively. A good agreement is noted between simulation and experimental results for the different test cases. To understand the importance of the size-effect parameters g_0^z and K^α on the overall evolution of variables, a sensitivity study was undertaken for the compression creep simulations through a $\pm 10\%$ variation of their evaluated values. The results, shown in Fig. 9a and b for g_0^z and K^α , respectively, demonstrate that the macro-

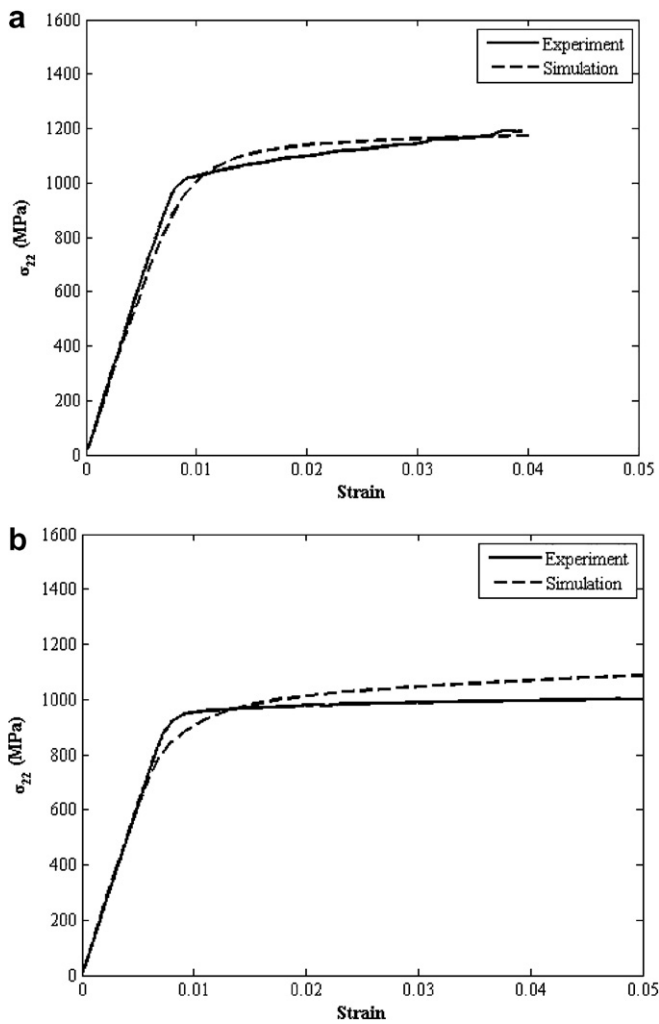


Fig. 7. Stress–strain plots validating the Ti-6242 computational model with experimental results for mechanical tests at: (a) constant compressive strain rate = $1.0 \times 10^{-4} \text{ s}^{-1}$ and (b) constant tensile strain rate = $1.0 \times 10^{-4} \text{ s}^{-1}$.

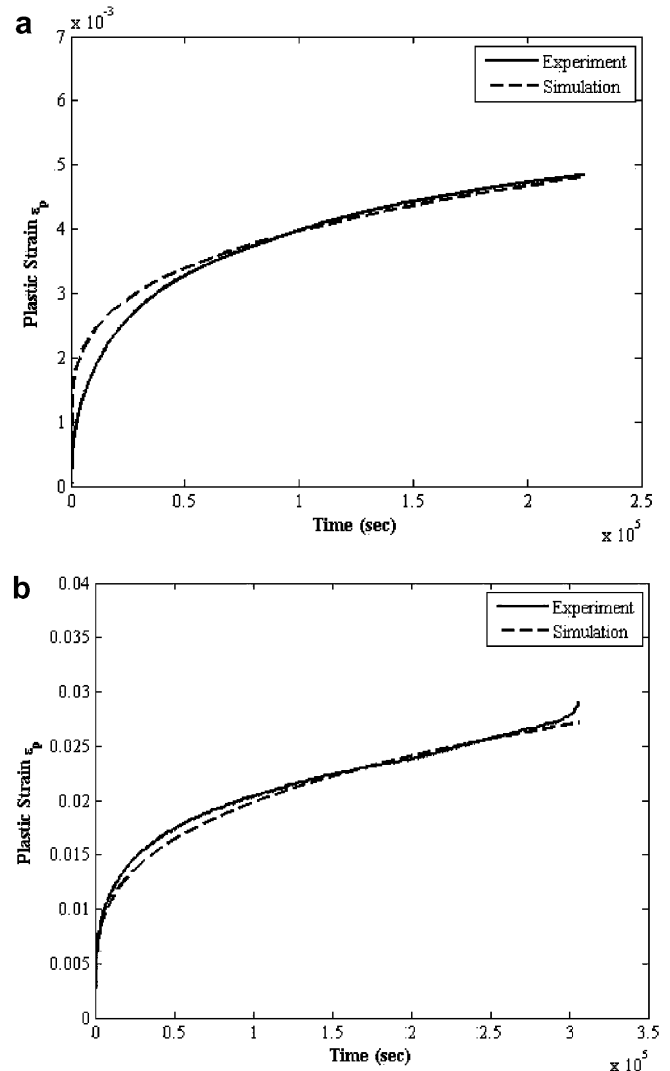


Fig. 8. Evolution of plastic strain in the Ti-6242 computational model, plotted with experimental results for creep test: (a) compression creep at a stress level of 907 MPa and (b) tension creep at a stress level of 897 MPa.

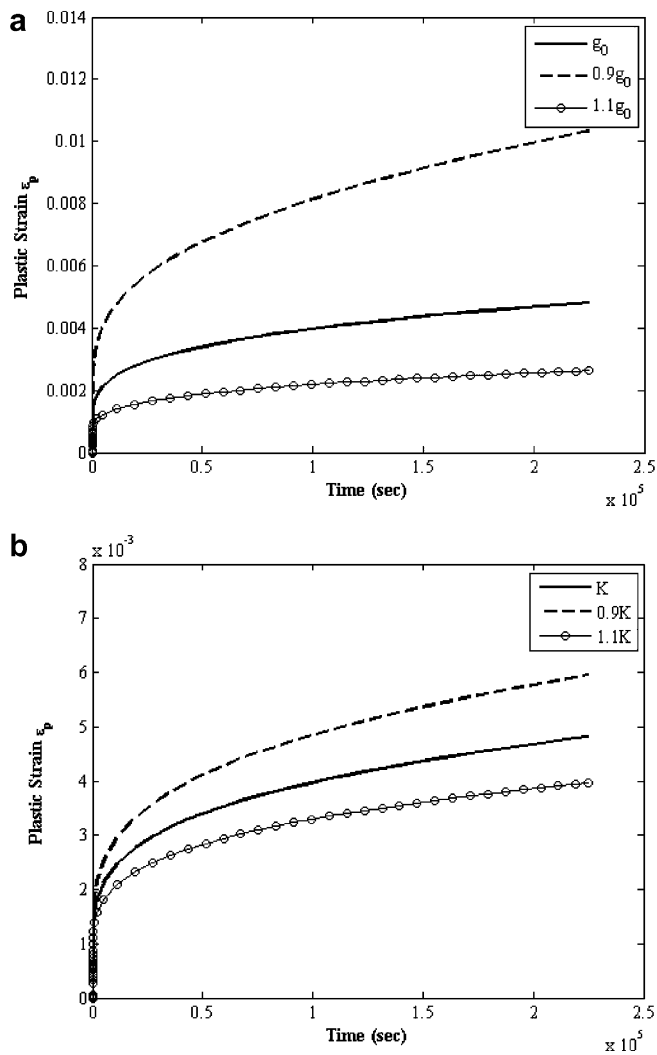


Fig. 9. Evolution of creep strain variation with time at a stress level of 907 MPa in compression for different values of the size-effect constants: (a) g_0 and (b) K .

scopic response is quite sensitive to changes in the values of these parameters.

4.2. Variation of macroscopic yield stress with grain size

The size-dependent crystal plasticity model is subsequently used to obtain a relationship between the macroscopic yield strength and grain/lath size of polycrystalline Ti-6242. Numerical simulations of constant strain rate tests were conducted with the FE model, in which the actual grain size was relevant. Various grain sizes between 10 and 200 μm were considered in the 70% (primary α)–30% (transformed β) polycrystalline aggregate, while keeping the α and β lath thicknesses constant. The macroscopic stress–strain response was evaluated for the various cases, and the macroscopic yield stress corresponding to 0.2% plastic strain is plotted as a function of the inverse square root of the average grain size in Fig. 10a. With increase in grain size, the macroscopic yield stress decreases and this

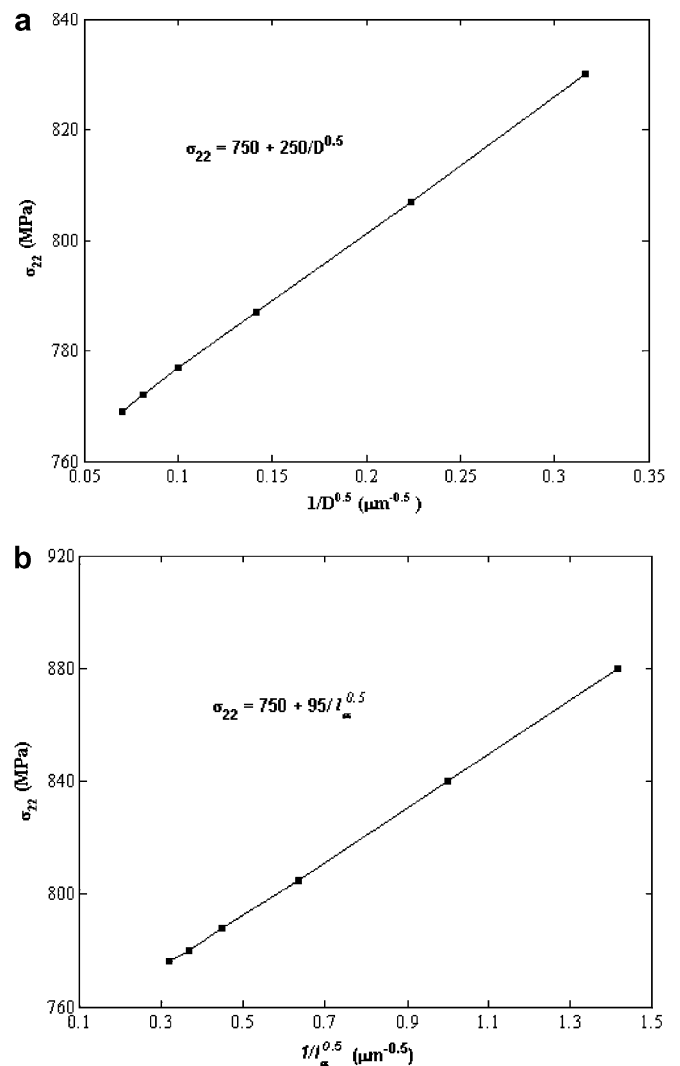


Fig. 10. Linear relationship between macroscopic yield stress of polycrystalline Ti-6242 and inverse of (a) the average grain size \sqrt{D} and (b) average lath α size $\sqrt{l_{\alpha}}$ in the transformed β region.

variation of yield stress is linear function of $1/\sqrt{D}$, where D is the average grain size of polycrystalline sample. The macroscopic size-effect constants σ_0 and K are obtained as 750 and 250 $\text{MPa}\sqrt{\mu\text{m}}$, respectively from a straight line fit. The K value is comparable to a value of 190 $\text{MPa}\sqrt{\mu\text{m}}$ reported for α -Ti at 78 K in Ref. [23].

Dependence of macroscopic yield strength on lath size is the subject of the next example. Polycrystalline samples with 100% transformed β phase (no primary α) are considered in this example with α lath thicknesses varying between 0.5 and 10 μm , but keeping the average grain size and β lath thickness constant. The macroscopic yield strength is plotted as a function of $1/\sqrt{l_{\alpha}}$ in Fig. 10b. The yield strength increases with decreasing lath thickness and a straight-line fit results in the macroscopic Hall–Petch constants σ_0 and K being 750 and 95 $\text{MPa}\sqrt{\mu\text{m}}$, respectively. This is comparable to the range of 20–50 $\text{MPa}\sqrt{\mu\text{m}}$ reported in Ref. [10] for two-phase Ti–6Al–4V at high temperatures for constant strain rate compression tests at

different strain rates. In Ref. [10], the α thickness was varied from 0.4 to 10 μm while keeping the β thickness constant. The K values in the present study are higher than those observed in experiments since the strain rate considered (10^{-4} s^{-1}) is much smaller than the range of strain rates considered in Ref. [10] ($0.1\text{--}10 \text{ s}^{-1}$). Experimental observations reveal a higher slope K for grain size dependence as compared to lath size dependence, which is also inferred with the present model. However, the grain size scale is of the order of 10–100 μm as compared to the lath size scale which is of the order of 0.1–10 μm . So the net effect of the size contribution term $\frac{K}{\sqrt{D}}$ may be more for lath size in comparison with grain size.

5. Effect of grain size on load shedding

The stress distribution in a polycrystalline microstructure can be highly non-uniform due to considerable dependence on grain orientation. Experiments employing electron back scattered diffraction (EBSD) technique in scanning electron microscopy (SEM) or OIM have shown that the relative strengths of neighboring grains are highly dependent on the orientation of basal planes with respect to the axis of loading [4]. This is because in the [0001] orientation, $\langle c+a \rangle$ dislocation slip on pyramidal slip systems is activated and this has a much higher critical resolved shear strength (CRSS) than the $\langle a \rangle$ type slip on basal or prismatic planes. This results in the local phenomenon of load shedding, due to $\langle a \rangle$ oriented grains, designated as soft grains, shedding load on to $\langle c+a \rangle$ oriented grains, designated as hard grains, with a significant rise in stress gradients across the interface. Such stress redistribution between microstructural regions with different strengths has been proposed as the fundamental cause of the development of faceted cracks [24]. Here, the terms “hard” and “soft”

grain are defined with respect to grain orientation and should not be confused with the hard and soft slip modes defined earlier. The load shedding response due to the varying crystallographic orientations of grains has been discussed in earlier papers [5,6,25,26]. The strength mismatch arising out of different grain orientations could be even more pronounced if the soft grain is larger than the neighboring hard grain. Thus it is very important to consider the size effect in the microstructural load shedding phenomenon.

To understand the effect of grain size on the load shedding phenomenon between soft and hard oriented grains, an FE model was constructed with two regions, namely an inner cube with a fine mesh of 1000 brick elements surrounded by an outer cube with a graded mesh of 6000 elements, as shown in the Fig. 11. For the grain in the inner region, the c -axis is aligned with the loading axis, while the c -axis is perpendicular to the loading axis for the grains in the surrounding region. Two different grain size units of 5 and 50 μm are considered with different a/b ratios, namely 0.1, 1.0 and 10, where ‘ a ’ and ‘ b ’ refer to the sizes of hard and soft grain, respectively. The two regions differ in their orientation and size. Creep simulations were carried out at an applied stress of 535 MPa. To facilitate comparison of stress gradients along the interface, the distance along the section XX shown in Fig. 11 is normalized such that the peak stresses lie at the same location for any grain size combination. The stress along the section XX is plotted for various cases after 1 and 10,000 s, from which the following observations can be made.

Fig. 12a shows the stress along XX after 1 s for a/b ratios of 0.1 and 10. In this plot, the stress in the soft grain away from the interface remains more or less constant, but drops near the interface to satisfy displacement compatibility with the hard grain. This results in high strain and stress

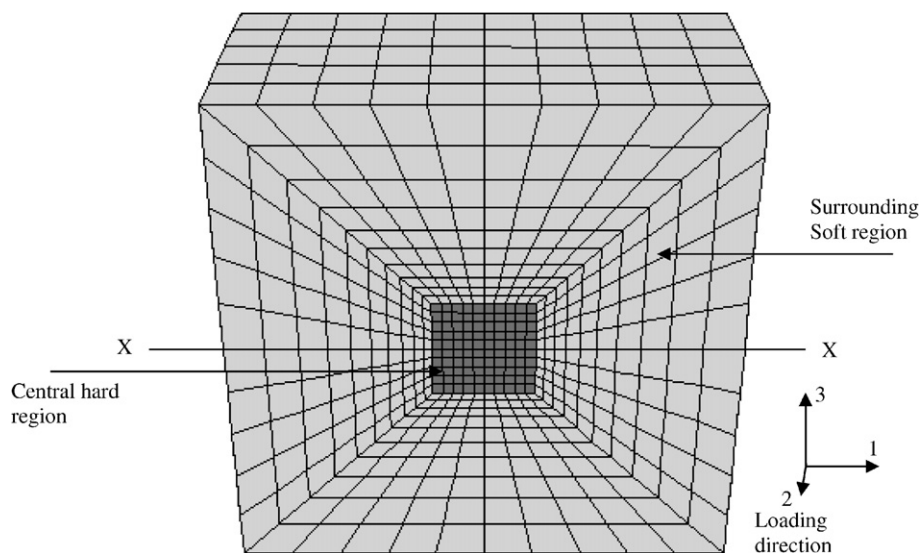


Fig. 11. FE model showing center hard region which has the ‘ c ’-axis aligned with the loading axis surrounded by soft region with prismatic slip active and loaded in two directions (perpendicular to the plane of the page).

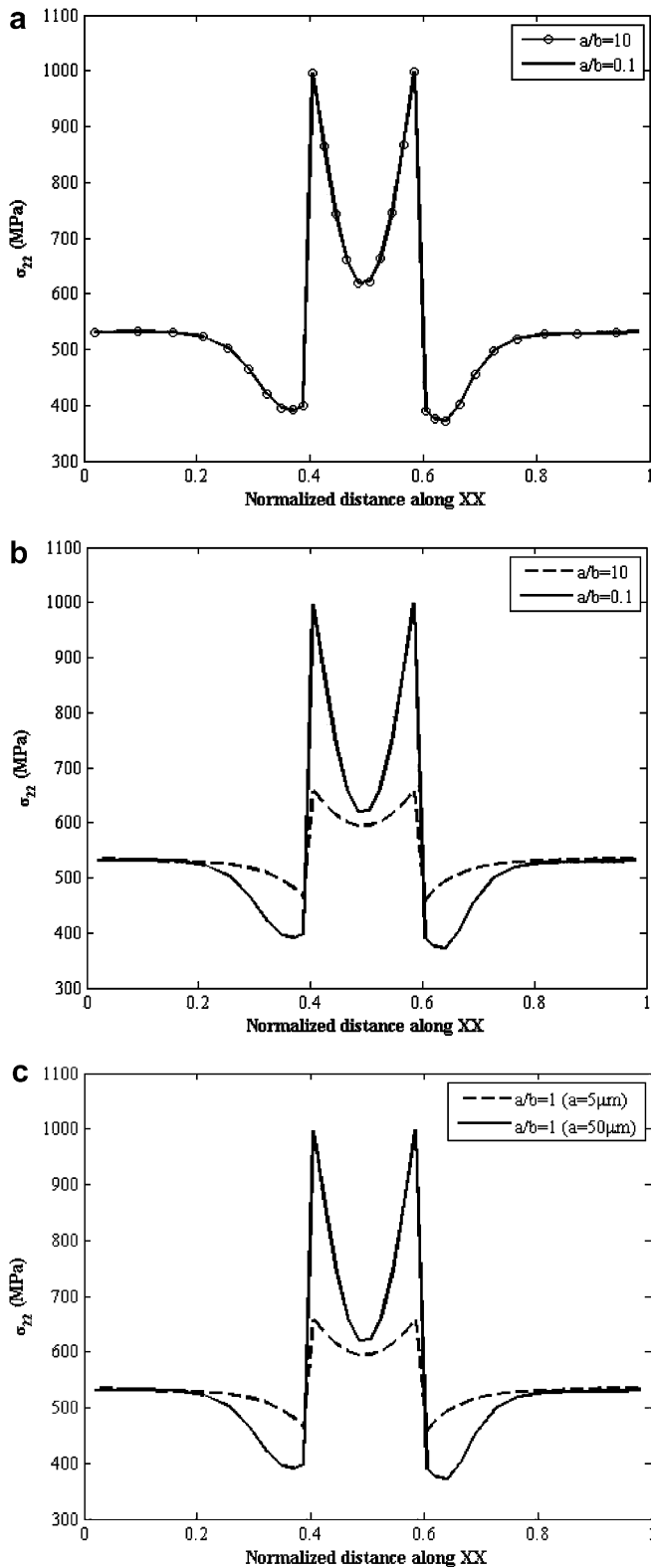


Fig. 12. Variation of stress (σ_{22}) along a section XX in a creep simulation at a stress level of 535 MPa for: (a) different size ratios after a creep time of 1 s; (b) different size ratios after a creep time of 10,000 s; and (c) same size ratio and different sizes after a creep time of 10,000 s.

in the hard grain at the interface compared to its center. Fig. 12b shows the stress along XX after a creep time of 10,000 s, corresponding to a/b ratios of 0.1 and 10. A com-

parison of Fig. 12a and b shows that the stress at all locations in the hard grain increases with time, while the stress in the soft grain continues to drop near the interface. From Fig. 12b it can be inferred that the soft oriented grains become much softer with the increase in grain size and the load shedding is more pronounced when the a/b ratio is 0.1 in comparison with a ratio of 10. Fig. 12c shows the stress along XX corresponding to an a/b ratio of 1.0 for two different grain sizes of 5 and 50 μm . For the same a/b ratio, the peak stress attained in the hard grain is much higher when the soft grains are larger. Also, a comparison of Fig. 12b and c shows that stress variation along XX is the same for a/b ratios of 1 and 10 when the size of the soft grain is 5 μm . The same is true for a/b ratios of 0.1 and 1 when the size of the soft grain is 50 μm .

From these results, it can be inferred that load shedding is dictated by the evolution of plastic strain in the soft grain and any change in its size significantly changes the peak stress in the hard grain. Varying the size of the hard grain, on the other hand, does not have any significant effect, since the $\langle c+a \rangle$ system has a much higher slip system deformation resistance compared with the basal or prismatic slip systems in the soft region. A change in size of the hard grain does not add much to the initial high values and has no significant effect on the load shedding behavior. This observation has important implications for microtextured regions, which tend to behave as a single large grain due to the ease of slip transmission between them, resulting from their nearly identical orientations. A large microtextured region with soft orientation adjacent to a hard grain will have a large effect on increasing the peak stress due to load shedding, while a microtextured hard region may not have a similar effect.

6. Morphology and texture effects for a real microstructure

In the FE modeling using idealized brick elements, the interface between the hard and soft regions is assumed to be flat, while in a realistic microstructure grains may be irregular with complex shapes. This introduces additional complexity with respect to stress evolution. This example is intended to study load shedding and stress concentration in a 3D simulated model of a real Ti-6242 microstructure. Incorporation of the size effect is necessary for modeling 3D real microstructures with accurate depiction of the grain morphology. Significant advances have been made in the second author's research group on 3D polycrystalline microstructure reconstruction and characterization [27–29] using data obtained from a dual-beam, focused ion beam SEM system. This system is able to acquire 3D orientation or EBSD data from a series of material cross-sections. This information has been successfully used [27–29] for automatic segmentation of individual grains from the image and translated into a 3D mesh used subsequently in FE analysis. Through a multitude of data sets, the intrinsic distributions of microstructural parameters can be captured and accurately

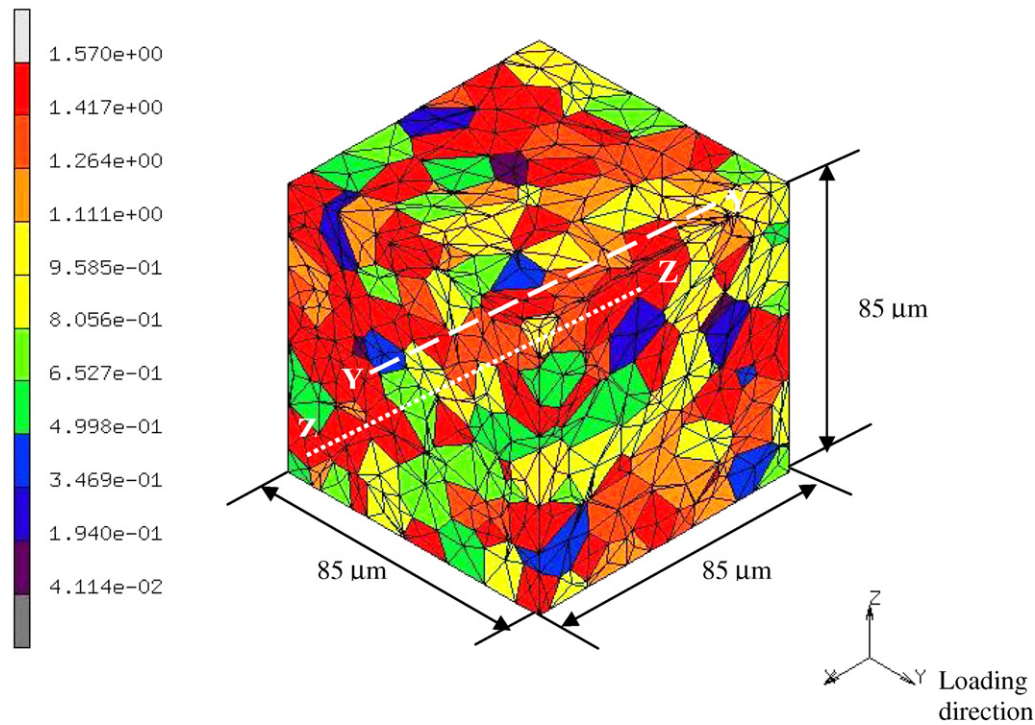


Fig. 13. 3D statistically equivalent microstructural FE model of polycrystalline Ti-6242, meshed with 3D tetrahedron elements. The colors represent the angle between the grain 'c'-axis and the loading axis in radians.

represented through 3D microstructure reconstruction. Computational tools have been developed [28,29] to create synthetic microstructures that are statistically equivalent to the measured structure. This methodology first uses 3D characterization to generate distribution functions of various microstructural parameters. Subsequently, a constrained Voronoi tessellation of the 3D region is executed, where the tessellation process is biased by statistics of the generated distributions. Crystallographic orientations are subsequently assigned to the grains using the OPAM, MPAM and MTPAM algorithms for orientation, misorientation and microtexture distributions, respectively. Such a synthetic microstructure is generated and meshed into a 3D FE mesh in the present study to understand the response of polycrystalline microstructures.

The FE model, shown in Fig. 13, has a large microtextured region of grains with their c -axes nearly aligned with the loading axis. The polycrystalline model has dimensions of $85 \times 85 \times 85 \mu\text{m}$ and consists of 500 grains that have orientation, misorientation, microstructure and size distributions statistically equivalent to those observed in OIM scans of a sample of Ti-6242. The model has 70% primary α and 30% transformed β grains. The slip system deformation resistances, g^α , of individual slip systems are obtained from the size-effect relationship Eq. (2), based on the grain size. All other crystal plasticity parameters have been calibrated in Ref. [5]. The 3D FE model is used to understand the significance of size, Schmid factor and

c -axis orientation on the load shedding response between hard and soft grains. The microstructural creep response is studied after 1 and 10,000 s, simulated for an applied load of 800 MPa in the 'y' direction as shown in Fig. 13. The local stress, σ_{22} , in the loading direction, Schmid factor, grain size and the c -axis orientation distribution are plotted along two representative sections, YY and ZZ, in Figs. 14 and 15, respectively. The sections are parallel to the x -axis and are at normalized (y, z) coordinates (0.1, 0.1) and (0.3, 0.2), respectively. As can be seen in Fig. 14a, the distribution of stress along YY, which passes through a microtextured hard region, is very non-uniform owing to the mismatch in strength from one grain to the next. The stress peaks are at **A**, **B** and **C**, while the valleys are at **D** and **E**. A comparison of stress variation along the section after 1 and 10,000 s shows that the stresses corresponding to the peaks (**A**, **B** and **C**) rise with time while those at **D** and **E** fall with time as a consequence of creep and load shedding from grains at **D** and **E** on to the corresponding grains at **A**, **B** or **C**. From the plots of the Schmid factor and the c -axis distributions in Fig. 14b and d, it is seen that point **A** corresponds to a hard grain with a low Schmid factor and c -axis orientation that is adjacent to a grain **D** with a high Schmid factor of 0.5. This results in a high Schmid factor mismatch and increased load shedding from the soft grain at **D** to the hard grain at **A**. The points **B** and **C** have a Schmid factor of ~ 0.4 and are adjacent to a grain at **E** with a high Schmid factor of 0.5. This mismatch also results in

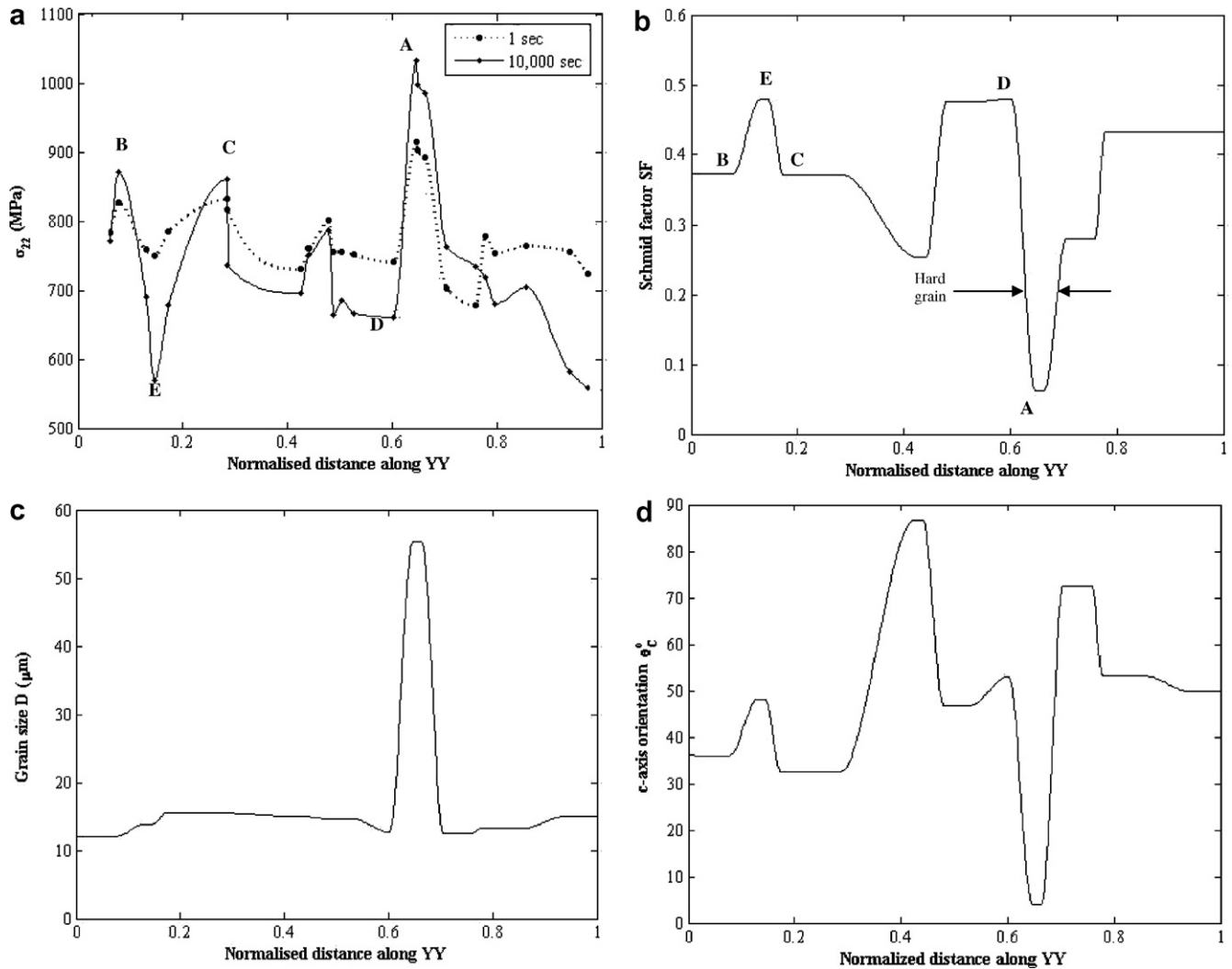


Fig. 14. Distribution of local variables: (a) loading direction stress (σ_{22}); (b) schmid factor; (c) grain size; and (d) 'c'-axis orientation, along a section YY parallel to the x -axis after creep times of 1 and 10,000 s and at a stress level of 800 MPa.

load shedding between grains having high and moderate $\langle a \rangle$ slip activity, but is not as pronounced as grains at region A, where load shedding is between $\langle a \rangle$ and $\langle c + a \rangle$ oriented grains. The plots along the section ZZ in Fig. 15 show that there is no steep increase in the stress with time in comparison to Fig. 14a. It can also be seen from Fig. 15a that there is no steep gradient in the stress σ_{22} due to the absence of $\langle c + a \rangle$ oriented grains. The Schmid factors of the grains vary between 0.3 and 0.5, resulting in moderate stress variation along this section. From these plots it can be concluded that a mismatch in Schmid factor results in load shedding between the grains that is predominant when there is a hard grain with $\langle c + a \rangle$ slip activity. With the realistic microstructure model, the effect of grain shape and irregularity of grain interfaces in stress and strain concentration can be accounted for in addition to texture and size effects. Such analysis, accounting for various microstructural parameters, is needed for establishing robust crack initiation criterion in polycrystalline Ti-6242 subjected to dwell fatigue.

7. Conclusions

The effect of microstructure size on the mechanical response of two-phase polycrystalline Ti-6242 alloy is studied in this paper. The model developed quantifies the dependence of grain and lath sizes and slip system deformation resistance of individual slip systems in a rate-dependent anisotropic elastic-crystal plasticity constitutive model. Three different characteristic lengths, namely the colony size, α lath thickness and β lath thickness, are used to incorporate the size effect in the transformed β phase, while the size effect in the primary α region is characterized by its grain size alone. Different slips are grouped as soft and hard slip modes, depending on the nature of slip transmission, and the characteristic length for each slip system is defined accordingly. The values of the constant slopes K_s^α and K_h^α , corresponding, respectively, to soft and hard slip modes in the Hall–Petch relationship, is calculated based on the dislocation pile-up model for various slip modes. The g_0^α values of individual slip systems, on the other hand, are obtained

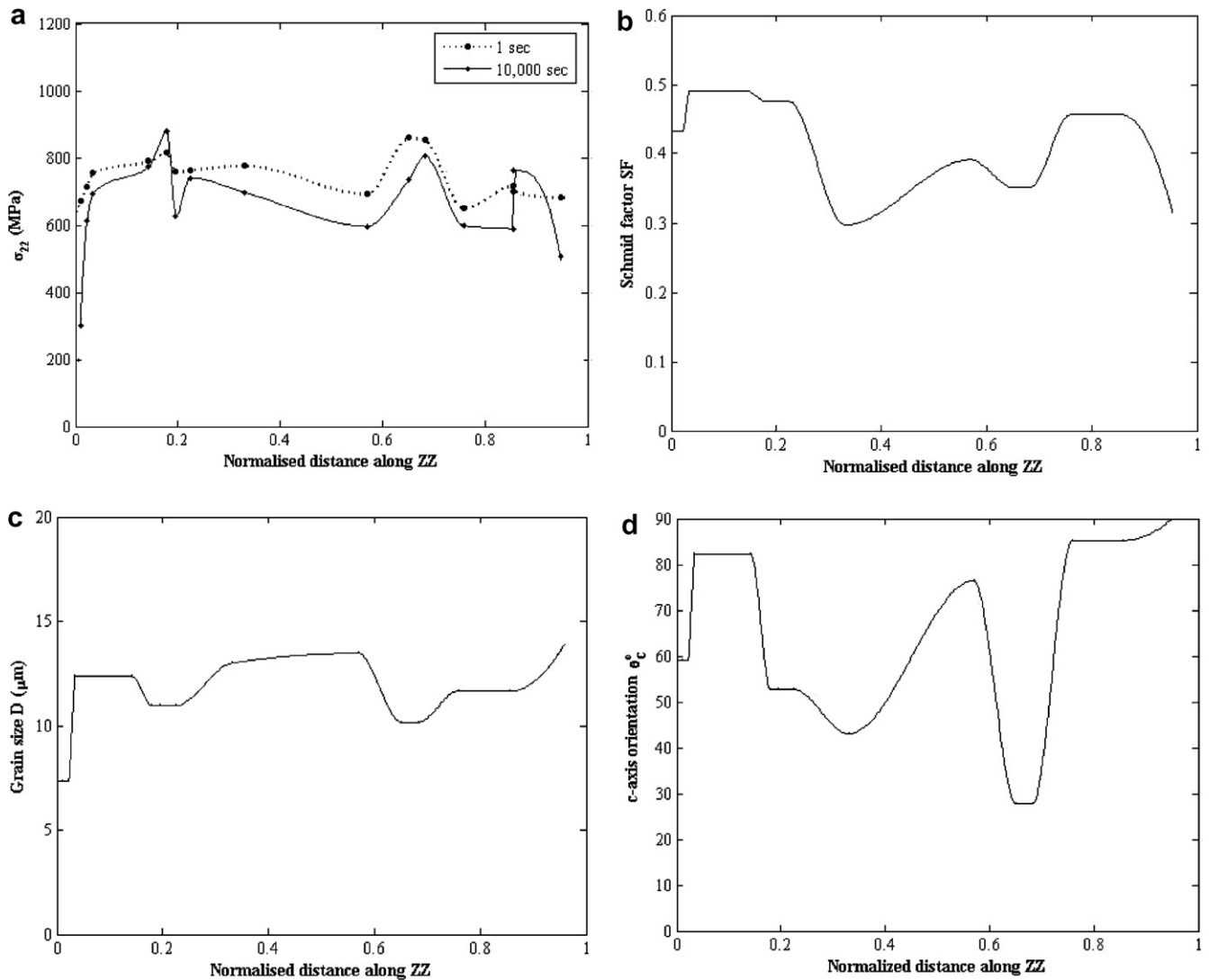


Fig. 15. Distribution of local variables: (a) loading direction stress (σ_{22}); (b) schmid factor; (c) grain size; and (d) 'c'-axis orientation, along a section ZZ parallel to the x-axis after creep times of 1 and 10,000 s and at a stress level of 800 MPa.

from the values, calibrated from corresponding single crystal and single colony experiments. A limiting lath thickness, below which the strength does not increase any further, is determined. The accuracy of the size-dependent model for polycrystalline Ti-6242 is established by comparing the simulation results for constant strain rate and creep tests in tension and compression with experiments. The effects of grain size and lath size on the macroscopic yield stress are studied through constant strain rate simulations for various grain and lath sizes. Linear relations are obtained between the yield strength and the inverse of \sqrt{D} and \sqrt{l} .

The validated model is then used to understand the effects of size and orientation mismatch on the load shedding between grains, which result in high stress gradients at the interface. To understand this phenomenon, the load shedding response is simulated in creep for various combinations of hard and soft grain sizes. It is seen that change in size of hard grains does not significantly change the load shedding response, since the size-effect contribution to

the slip system resistance is small compared to its initially high value. However, a change in the size of the soft grains considerably changes the peak stress due to load shedding. Finally, the effect of microstructural morphology on local stresses is studied through FE simulations of a 3D simulated microstructure that is statistically equivalent to a real Ti-6242 polycrystalline microstructure. The evolution of stress with creep along different sections of the microstructure is studied and analyzed against local microstructural characteristics. A mismatch in Schmid factor results in load shedding between the grains that is predominant when there is a hard grain with $\langle c+a \rangle$ slip activity. No stress gradient is observed in the section with no hard grain orientation. This study emphasizes the importance of realistic representation of the effects of grain size and shape on load shedding. In conclusion, the size-dependent crystal plasticity model established in this study has the capability to quantify the effects of various microstructural parameters and can be used for further study of critical combinations

of these parameters that would result in localized fracture in Ti-6242 microstructures under dwell fatigue loading.

Acknowledgements

The authors are grateful to Professors Jim Williams, Mike Mills and Stan Rokhlin and Dr. Vikas Sinha for providing guidance on this work and all the experimental data. This work has been supported by the Federal Aviation Administration through Grant No. DTFA03-01-C-0019 (Program Director: Dr. Joe Wilson). This support is gratefully acknowledged. The authors gratefully acknowledge the software support provided by Drs. Sanjay Choudhry and Shiva Padmanabhan of MSC MARC. The authors acknowledge the insightful suggestions of Drs. A. Woodfield, A. Chatterjee, J. Hall, J. Schirra and M. Savage on various aspects of this work. Computer support by the Ohio Supercomputer Center through Grant No. PAS813-2 is also acknowledged.

References

- [1] Froes FH, editor. Non-aerospace applications of titanium. Warrendale (PA): TMS; 1998.
- [2] Imam MA, Gilmore CM. Metall Trans A 1979;10:419.
- [3] Suresh S. Fatigue of materials. Cambridge: Cambridge University Press; 1991.
- [4] Bache MR. Int J Fatigue 2003;25:1079.
- [5] Deka D, Joseph DS, Ghosh S, Mills MJ. Metall Trans A 2005;37:1371.
- [6] Hasija V, Ghosh S, Mills MJ, Joseph DS. Acta Mater 2003;51:4533.
- [7] Hall EO. Proc Phys Soc London 1951;64:747.
- [8] Petch NJ. J Iron Steel Inst 1953;174:25.
- [9] Cao G, Fu L, Lin J, Zhang Y, Chen C. Intermetallics 2000;8:647.
- [10] Semiatin SL, Bieler TR. Acta Mater 2001;49:3565.
- [11] Maruyama K, Yamada N, Sato H. Mater Sci Eng A 2001;319–321:360.
- [12] Norfleet D. The Ohio State University: Columbus (OH), unpublished research; 2005.
- [13] Savage MF, 2000, “Microstructural and mechanistic study of low temperature creep and dwell fatigue in single colony alpha/beta titanium alloys.” Ph.D. dissertation. Columbus (OH): OSU.
- [14] Suri S, Vishwanathan GB, Neeraj T, Hou DH, Mills MJ. Acta Mater 1999;47:1019.
- [15] Kalidindi SR, Bronkhorst CA, Anand L. J Mech Phys Solids 1992;40:537.
- [16] Kothari M, Anand L. J Mech Phys Solids 1998;46:51.
- [17] Harren S, Lowe TC, Asaro RJ, Needleman A. Philos Trans R Soc London A 1989;328:443.
- [18] MSC-MARC reference manuals., 2005, MSC Software Corporation: Santa Anna (CA).
- [19] Savage MF, Tatalovich J, Mills MJ. Mater Sci Eng A 2004;84(11):1127.
- [20] Li J, Chou Y. Metall Trans 1970;3:1145.
- [21] Eshelby JD. Phys Status Solidi 1963;3:2057.
- [22] Neeraj T, Savage MF, Tatalovich J, Kovarik L, Hayes RW, Mills MJ. Philos Mag 2005;85(2–3):279.
- [23] Meyers MA, Vohringer O, Lubarda VA. Acta Mater 2001;49:4025.
- [24] Sinha V, Spowart JE, Mills MJ, Williams JC. Metall Mater Trans A 2006;37:1507.
- [25] Xie CL, Ghosh S, Groeber M. J Eng Mater Tech 2004;126:339.
- [26] Venkataramani G, Deka D, Ghosh S. J Eng Mater Tech ASME 2006;128:356.
- [27] Bhandari Y, Sarkar S, Groeber M, Uchic MD, Dimiduk DM, Ghosh S., Comp Mater Sci, in press.
- [28] Groeber M, Uchic MD, Dimiduk DM, Bhandari Y, Ghosh S. In: Proceedings of Multi-scale materials modeling, Freiburg, Germany, 2006.
- [29] Groeber M, Ghosh SM, Uchic MD, Dimiduk DM, Bhandari Y., submitted.